

Pivotal role of H₂ in the isomerization of isosorbide over Ru/C catalyst

H. Hu,^{a,b1} A. Ramzan,^{c1} R. Wischert,^b F. Jérôme,^a C. Michel,^{c*} K. de Olivera Vigier,^{a*} M. Pera-Titus^{b*}

^a *Eco-Efficient Products and Processes Laboratory (E2P2L), UMI 3464 CNRS – Solvay, 3966 Jin Du Road, Xin Zhuang Ind. Zone, 201108 Shanghai, China*

^b *IC2MP UMR CNRS_ Université de Poitiers 7285, ENSIP 1 rue Marcel Doré, TSA 41195, 86073 Poitiers Cedex 9, France*

^c *Univ Lyon, Ens de Lyon, CNRS UMR 5182, Université Claude Bernard Lyon 1, Laboratoire de Chimie, F69342 Lyon, France*

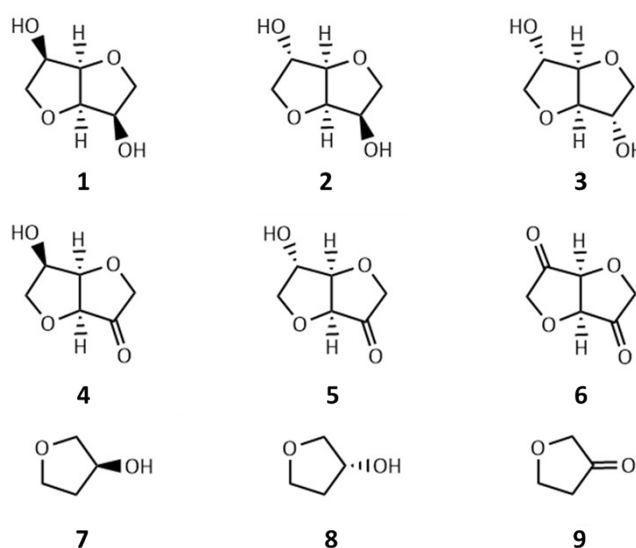
¹ *These authors contributed equally to the work*

**Corresponding authors: marc.pera-titus-ext@solvay.com, karine.vigier@univ-poitiers.fr, carine.michel@ens-lyon.fr*

Experimental Section

Chemicals

1, 4: 3, 6-dianhydro-D-mannitol denoted as isomannide (**1**), 1, 4: 3, 6-dianhydro-D-glucitol denoted as isosorbide (**2**), 1, 4: 3, 6-dianhydro-D-iditol denoted as isoidide (**3**), (3a*S*, 6*S*, 6a*R*) -6-hydroxytetrahydrofuro [3, 2-*b*] furan-3 (2*H*) -one denoted as endo-OH monoketone (**4**), (3a*S*, 6*R*, 6a*R*) -6-hydroxytetrahydrofuro [3, 2-*b*] furan-3 (2*H*) -one denoted as exo-OH monoketone (**5**), 1, 4: 3, 6-dianhydro-D-threo-2, 5-hexodiulose denoted as isohexide diketone (**6**), (R)-(-)-3-Hydroxytetrahydrofuran denoted as endo-OH THF (**7**), (S)-(+)-3-Hydroxytetrahydrofuran denoted as exo-OH THF (**8**), Dihydrofuran-3(2*H*)-one denoted as THF ketone (**9**).



Isoidide (98 %) was purchased from FluoroChem. Isosorbide (98 %), isomannide (95 %), endo-OH THF (98 %), exo-OH THF (99 %), THF ketone (97 %), deuterium oxide (99.9 %), DMSO (99.9 %) and the solvents: methanol (99.8 %), ethanol (99.8 %), 1-butanol (99.4 %), 1-pentanol (99 %), isopropanol (99.9 %), *t*-amyl alcohol (99 %) were procured from Sigma-Aldrich. Unless stated otherwise, all chemicals were used without any further purification. Activated carbon supported ruthenium (Ru/C, 5 wt%, reduced) catalyst was purchased from Sigma-Aldrich. Activated carbon supported platinum (5 wt%) and bismuth (Pt-Bi/C, 1.5 wt%) catalyst was purchased from Johnson&Matthey.

General procedure for the synthesis of isohexide ketone intermediates

The oxidation of isohexides was performed in a 50 mL double-neck flask. Typically, 1g substrate, 15 mL H₂O and 0.2 g Pt-Bi/C were added to the flask. Air flow (80 mL/min) was introduced to the suspension and the reaction temperature was set to 60 °C. The exo-OH monoketone **5** and diketone **6** could be obtained after 72 h starting from isosorbide and isomannide at full conversion, respectively.

General procedure for epimerization reactions

The isomerisation reactions were carried out in a Parr reactor (75 mL) equipped with a thermocouple and a digital manometer. Typically, 1 g substrate, 15 mL H₂O and 0.05 g Ru/C were added to the reactor. The reactor was then sealed, flushed 3 times with H₂ and sealed at the target H₂ pressure and temperature. After the reaction, the reactor was cooled down to room temperature using an ice-water mixture and the internal pressure was released. The crude product was filtered (0.2 μm) to remove the

catalyst and diluted in methanol. The mixture was analysed by gas chromatography using a Bruker Scion 436 GC equipped with an Agilent HP-5MS column (30 m x 0.25 mm x 0.25 μ m) and a flame ionization detector (FID). In a typical analysis, the sample was subjected to 100 °C for 1 min and heated to 250 °C at 10 °C.min⁻¹. At these conditions, the retention time (min) of the different reagents was: **(1)** 7.8; **(2)** 8.6; **(3)** 9.5; **(4)** 8.0; **(5)** 8.6; **(6)** 7.3; **(7)** 3.6; **(8)** 3.6 and **(9)** 3.0 min. In the isomerisation of 3-OH-THF, a MCP-100 Anton Paar polarimeter (cell length 100 mm, 25 °C) was used to determine the ratio between compound **7** and **8**. Additional analyses were carried out by ¹H NMR on a 400 MHz Bruker spectrometer using D₂O as solvent (residual signal at 4.7 ppm).

General procedure for the measurement of H₂ solubility in D₂O by NMR

A pressurized NMR tube (524-PV-7, maximum pressure 300 p.s.i.) was purchased from Wilmad-Labglass. The gas pressure was monitored by a digital monometer when charged gas. The topshim of the NMR tube was conducted without rotation before the NMR measurement was recorded on a 400 MHz Bruker spectrometer (Relaxation time D=5 s and scan number=64 in order to keep a good spectrum quality). The H₂/DMSO was calculated using the division of H₂ (signal/noise) by DMSO (signal/noise).

Computational Details

Periodic Density Functional Theory (DFT) as implemented in the Vienna Ab initio Simulation Package (VASP) was used to investigate the reaction pathways for the isomerisation of *endo*-OH and *exo*-OH functional groups in isosorbide.¹ Electronic energies were approximated at the GGA level using the Perdew-Burke-Ernzerhof (PBE)² exchange-correlation functional with dDSc dispersion correction.³ Ion-electron interactions were treated using Projector Augmented Wave (PAW)^{4,5} formalism with 850 eV cutoff for the augmentation charges and all plan-waves with energy lower than or equal to 500 eV were included in the basis set. The Ru catalyst was modeled by a 4 layered thick p(4 × 4) slab of Ru(0001) surface. Full optimization of the Ru bulk was performed resulting in bulk parameters of a = 2.702 Å and c/a = 1.578 in good agreement with the experimental values.⁶ The bottom 2 layers were kept frozen to their bulk positions; all other degrees of freedom were allowed to relax until all force components were less than 0.01 eV/Å. The cutoff for the electronic self-consistency cycle was set to 1×10⁻⁷ eV. All calculations used a Gamma-centered 5 × 5 × 1 k-point mesh to sample the Brillouin zone and second order Methfessel-Paxton smearing scheme was employed with a smearing width of 0.2 eV. To minimize the interactions between different periodic copies of the system in the direction normal to the slab, a minimum vacuum gap of 25 Å augmented by a dipole correction to both energy and forces in that direction was employed.

Thermal and entropic contributions to the total energy were estimated under the harmonic approximation by calculating the normal modes for the adsorbate part of all reaction species using the central finite differences with step size of 0.01 Å. All normal modes (those below 50 cm⁻¹ were rescaled to 50 cm⁻¹) were used to calculate the zero-point energy (ZPE) and other thermal and entropic contributions under ideal gas approximation.

The molecular species were optimized at Gamma point in a 20 × 20 × 20 cubic box. Due to polarity of the molecules, dipole correction was used in all directions. A reduced smearing width of 0.02 eV was employed for molecular species. The vibrational, rotational and translational contributions to the enthalpy and entropy were calculated under harmonic ideal gas approximation taking into account proper symmetry of the molecules.

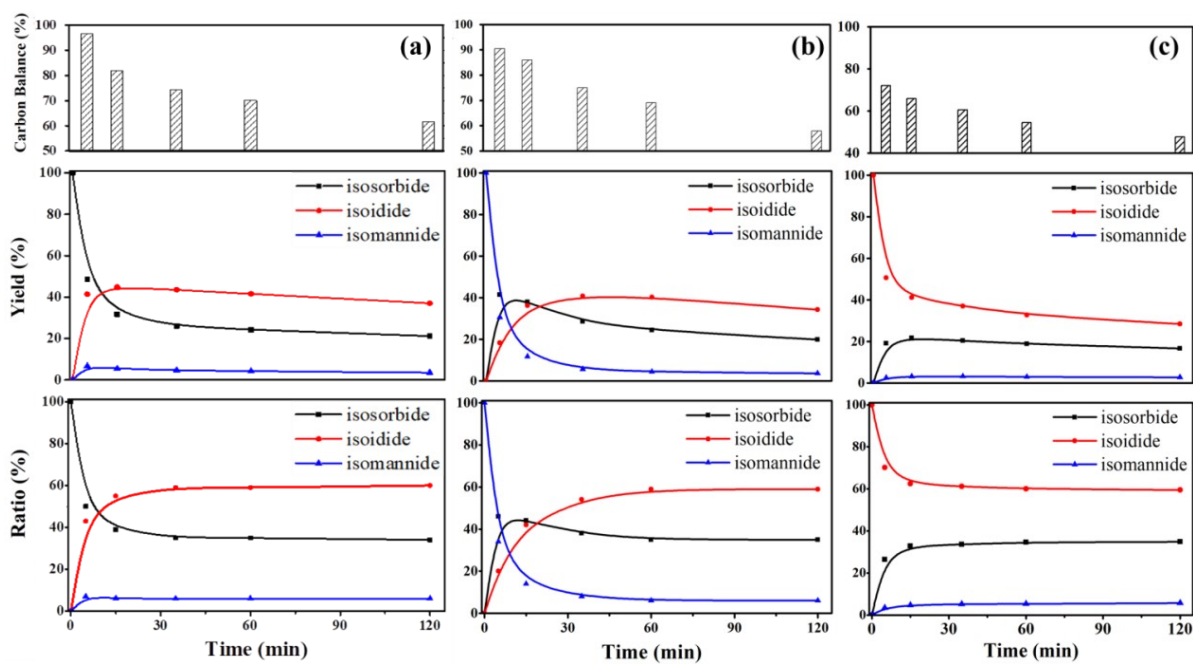


Fig S1. (Top) Carbon balance, (middle) yield and (bottom) ratio of isomers upon isomerisation of: (a) IS, (b) IM and (c) II. Reaction conditions: 1 g substrate, 15 mL H₂O, 0.05 g Ru/C (5wt %), 31 bar H₂, 200 °C.

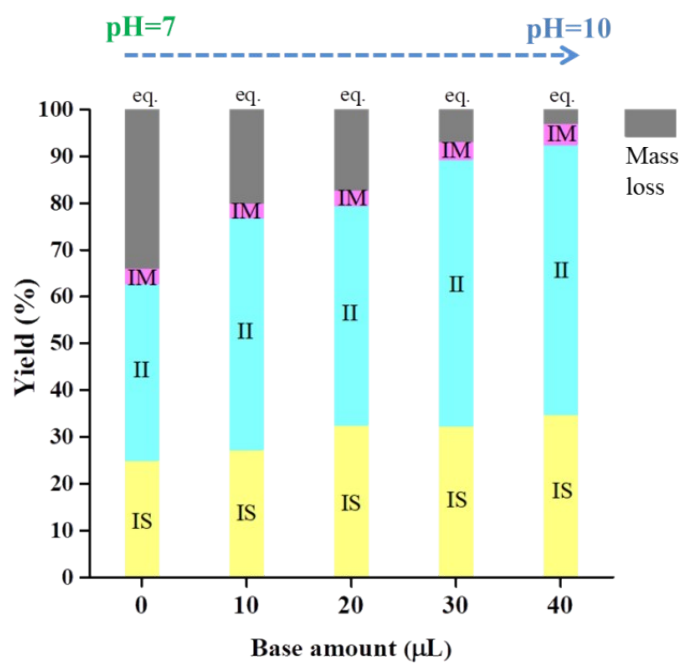


Fig S2. Product distribution and mass loss using different amounts of NaOH solution. Reaction conditions: 1 g IS, 15 mL H₂O, 0.5 mol/L NaOH, 0.05 g Ru/C (5wt %), 31 bar H₂, 200 °C, 1 h.

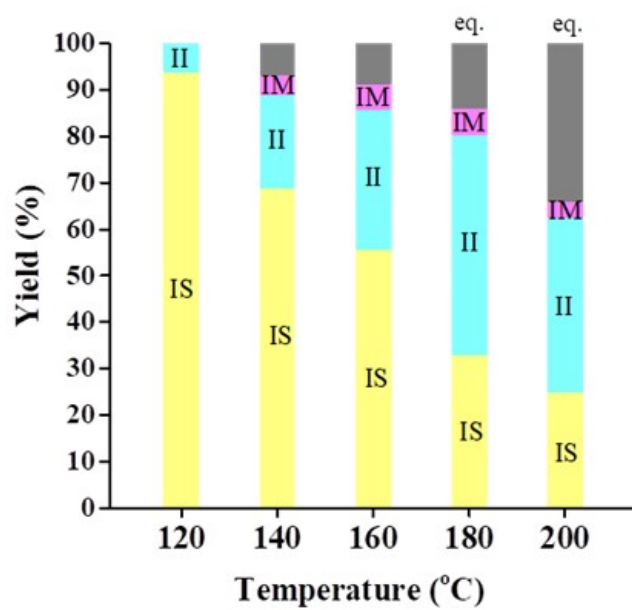


Fig S3. Product distribution and mass loss at different temperatures. Reaction conditions: 1 g IS, 15 mL H₂O, 0.05 g Ru/C (5wt %), 31 bar H₂, 1 h.

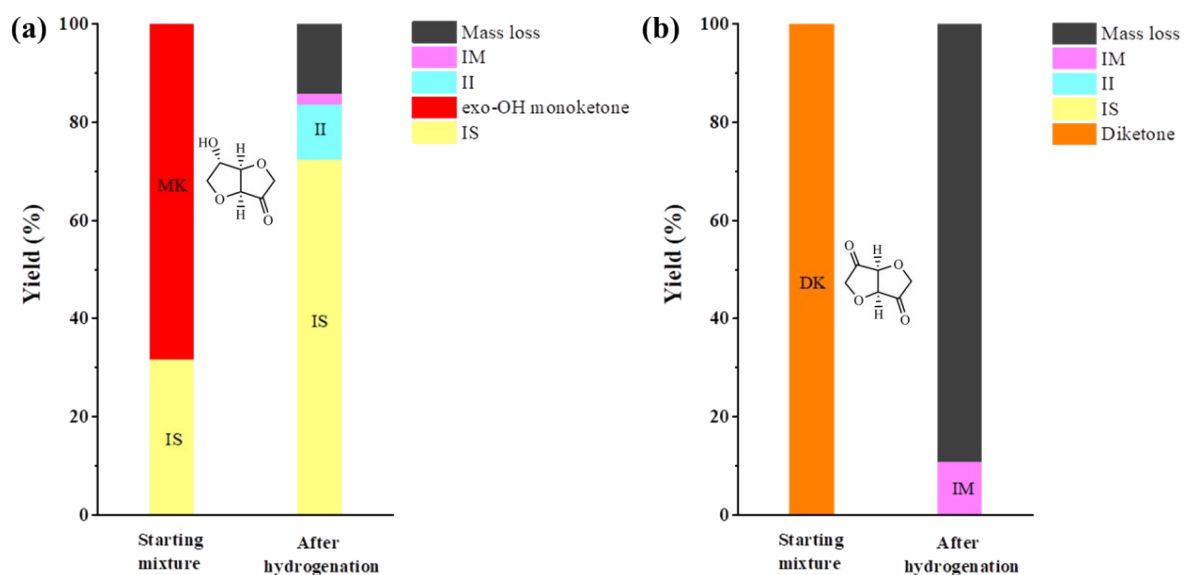


Fig S4. (a) Hydrogenation of *exo*-OH monoketone and IS mixture. Reaction conditions: 1 g mixture, 15 mL H₂O, 0.05 g Ru/C (5wt %), 10 bar H₂, 100 °C, 1 h. (b) Hydrogenation of isohexide diketone. Reaction conditions: 1 g diketone, 15 mL H₂O, 0.05 g Ru/C (5wt %), 50 mL/min H₂ flow, 25 °C, 10 min.

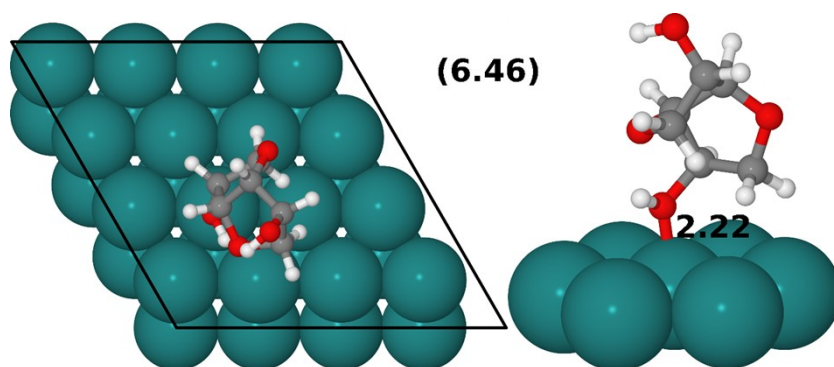


Fig S5. Vertical adsorption configuration of IS through its *endo*-OH group. The O atom of OH group is chemisorbed on Ru with bond-length of 2.22 Å and has free energy of adsorption equal to 6.46 kJ.mol⁻¹.

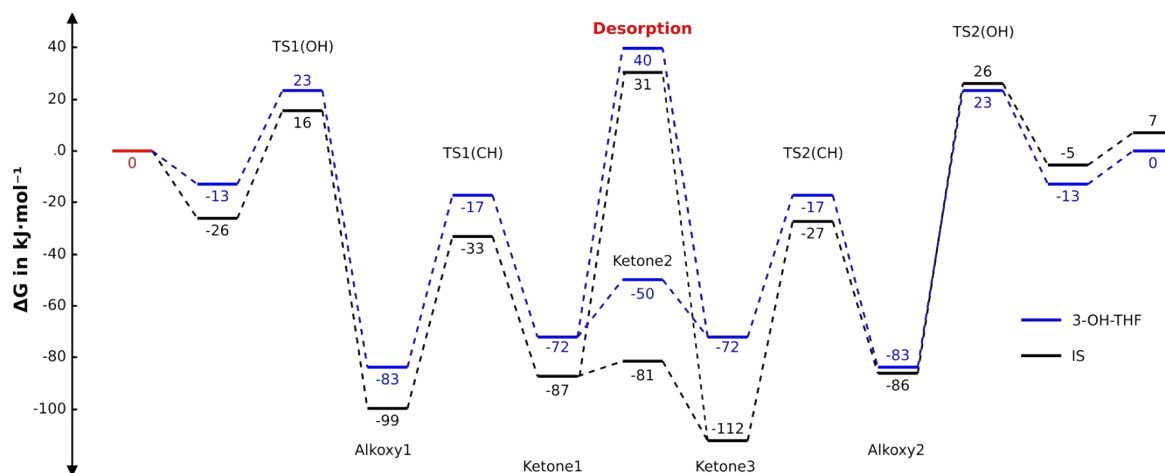
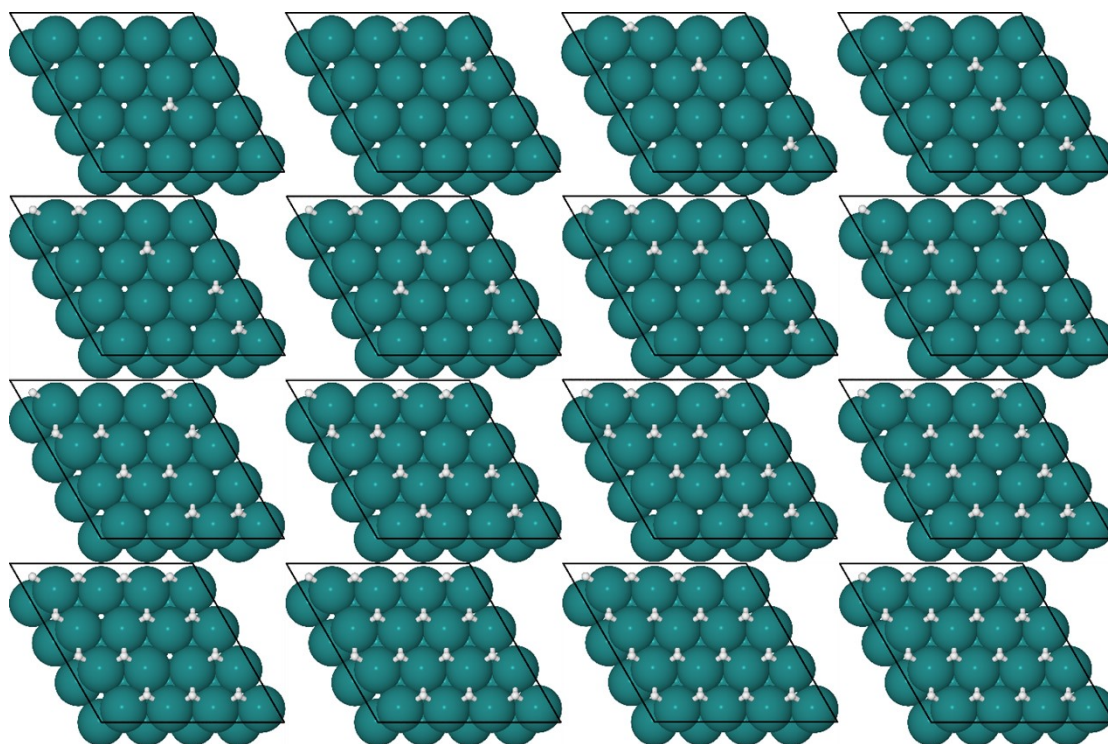


Fig S8. Comparison of dehydrogenation/rehydrogenation pathways of IS (**Endo2Exo**) and **3-OH-THF**. The ketone intermediates of **3-OH-THF** lie higher than those of IS by almost 40 kJ.mol⁻¹. The desorption values represent the full desorption of ketone and hydrogen molecule leaving behind clean catalyst surface. The pathway for **3-OH-THF** is mirror symmetric around the desorption point i.e. **TS1(OH)** and **TS2(OH)** are same for **3-OH-THF**.

a)



b)

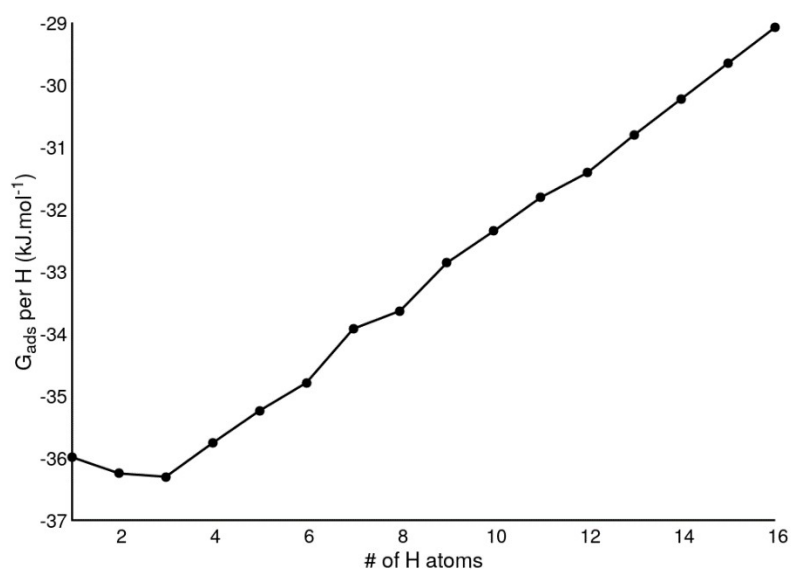


Fig S7. (a) Most stable distribution of H on Ru(0001) surface up to 1 ML. H preferentially binds to three-fold fcc hollow sites. The shown distributions were found after checking all possible combinations of given number of H atoms over p(4x4) supercell i.e. 16 fcc sites. **(b)** Trend of Gibbs free energy of adsorption per H atom on Ru(0001) up to 1 ML. Normal modes for the adsorbed H atoms were used to calculate ZPVE and other enthalpic and entropic contributions under harmonic approximation at 160 °C and 1 atm pressure.

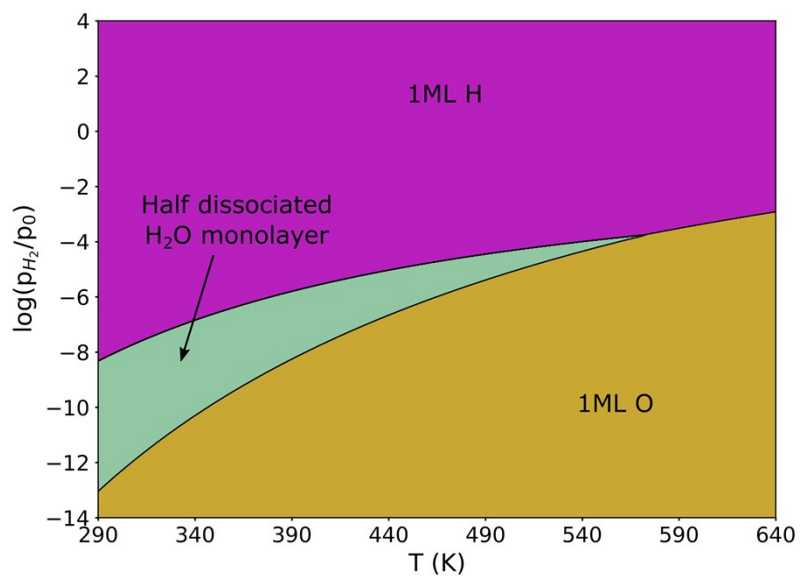


Fig S8. Predominance diagram of O, H, OH, H₂O on Ru(0001) in function of the pressure of H₂ and the temperature, using the saturation vapor pressure of water as a reference of the chemical potential of O. It includes the following structures: (i) monolayer of H (see Fig. S7) (ii) monolayer of OH (iii) monolayer of O (iv) monolayer of water (v) monolayer of mixed OH/H₂O as proposed by Feibelman.⁷

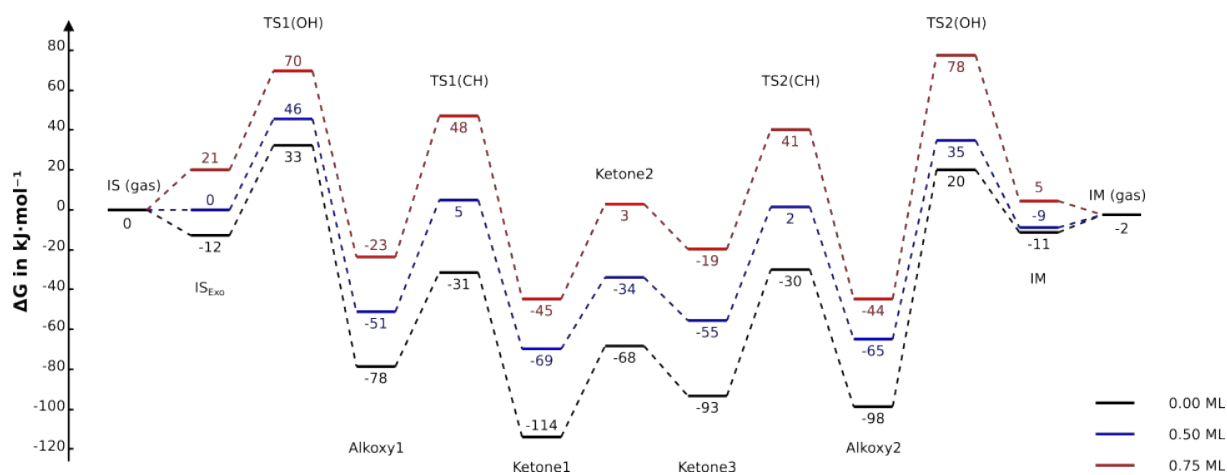
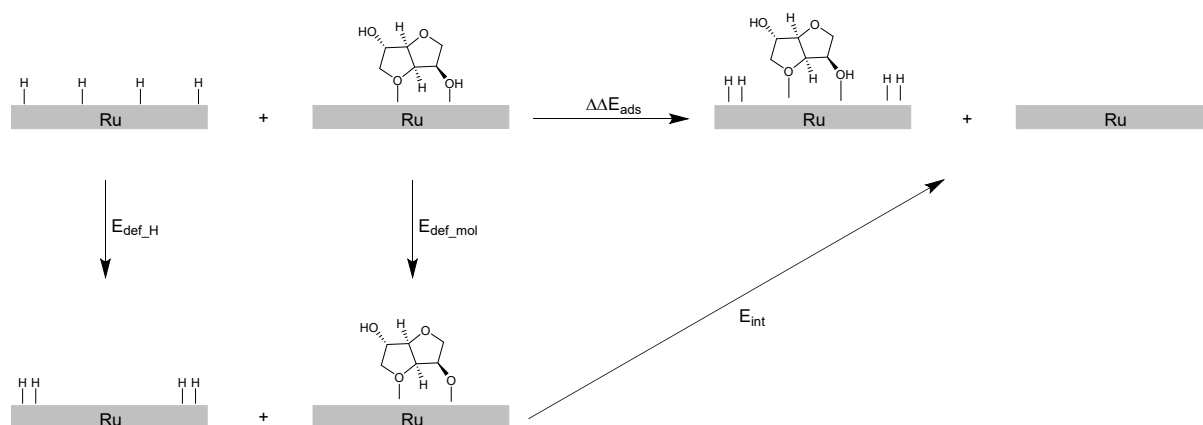


Fig S9. Free energy profiles for the **Exo2Endo** pathway at different coverage of co-adsorbed H. The enthalpic and entropic contributions to the free energy were calculated using ideal gas harmonic approximation at 160 °C and 1 atm pressure.

Deformation-Interaction Analysis

Scheme S1 gives the overall protocol adopted for the deformation-interaction analysis. The species on the top-left side of the horizontal arrow represent the most stable, fully optimized adsorption geometries of H, at 0.5 ML or 0.75 ML coverage, and the molecular species on separate slabs with zero co-adsorption. The species on the top-right signify the fully optimized co-adsorbed geometry of reaction intermediates and transition states along with the corresponding number of H atoms and the pristine, fully relaxed Ru(0001) slab. The corresponding energies for these species are known from our pathway investigation and are given in **Fig 6** (main text) and **Fig S9**. The species at the bottom, however, represent the deformed geometries relative to the fully optimized geometries at the top-left and are obtained after removing the molecule or the co-adsorbed H atoms from the fully optimized co-adsorbed geometry shown on top-right.



Scheme S1. Schematic of the deformation-interaction analysis performed for all reaction species under 0.50 ML and 0.75 ML co-adsorbed H.

The change in adsorption energy upon co-adsorption, denoted by $\Delta\Delta E_{ads}$ in Schem S1, can be written as follows:

$$\Delta\Delta E_{ads} = E_{def_mol} + E_{def_H} + E_{int} \quad (S1)$$

where E_{int} represents the interaction energy and E_{def_mol} , E_{def_H} are the deformation energies corresponding to the deformation experienced by the molecular species and the H atoms co-adsorbed on the surface, respectively. The latter two quantities were calculated by running Single Point energy calculations at the same level of theory as described before.

The calculated contributions to the $\Delta\Delta E_{ads}$ for four different possible scenarios are plotted in **Fig S10**.

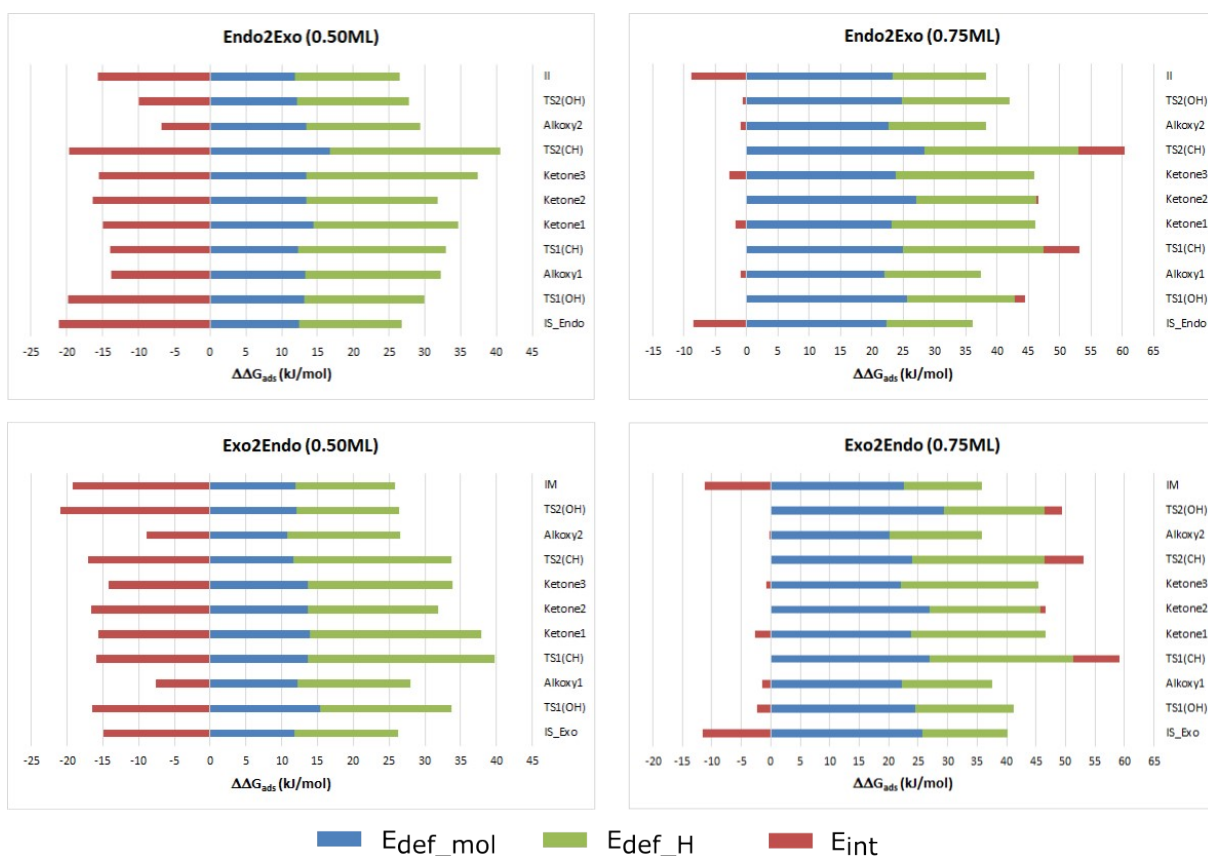


Fig S10. The plots of deformation and interaction energies for all the reaction intermediates and transition states at 0.5 ML and 0.75 ML coverage of H.

H₂ solubility measured by NMR

Temperature effect:

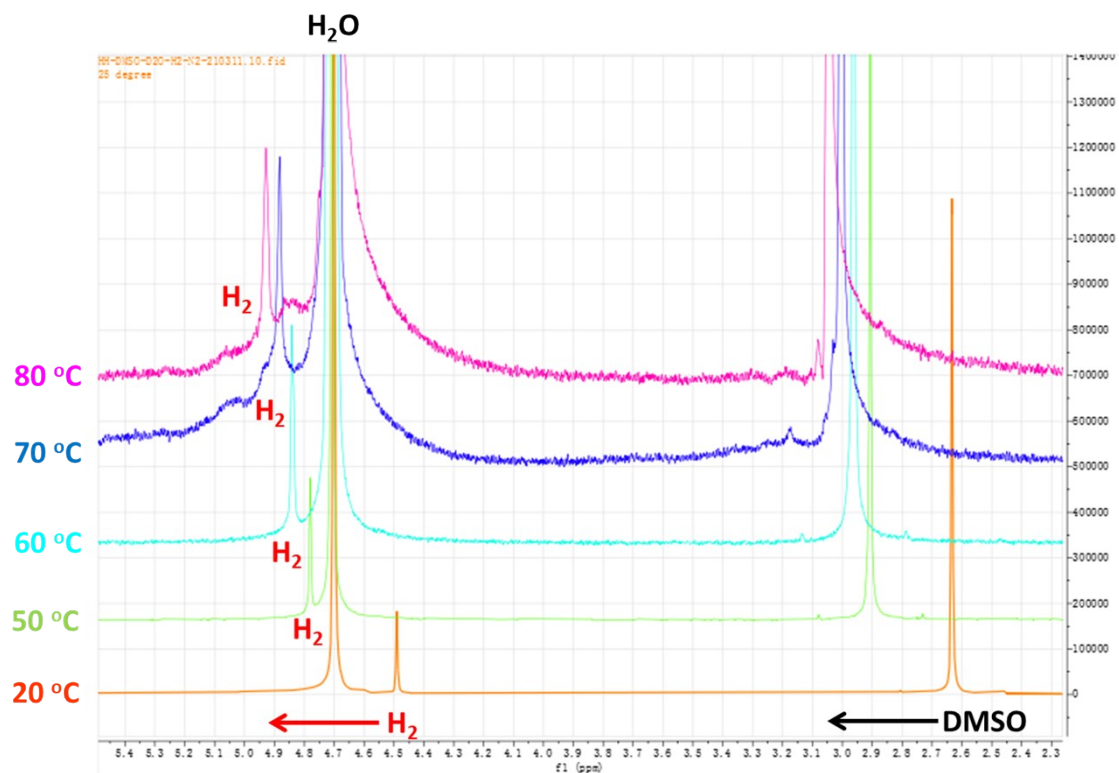


Fig S11. NMR spectra of dissolved H₂ in D₂O as a function of temperature using DMSO as internal standard.

It can be seen from the results that the peaks attributed to H₂ and DMSO shifted to higher value with the increase of temperature, which is consistent with the literature.⁸ Due to the static dissolution of H₂ in D₂O, it is difficult to make sure the equilibrium is reached when increasing temperature. The influence of temperature on the signal cannot be measured accurately under current conditions. Therefore, the H₂ solubility at different temperatures was not compared. When the temperature is increased to 70 and 80 °C, a poor spectra quality was obtained even the parameters had been optimized. 20 and 50 °C were used in the following measurements.

Effect of stirring

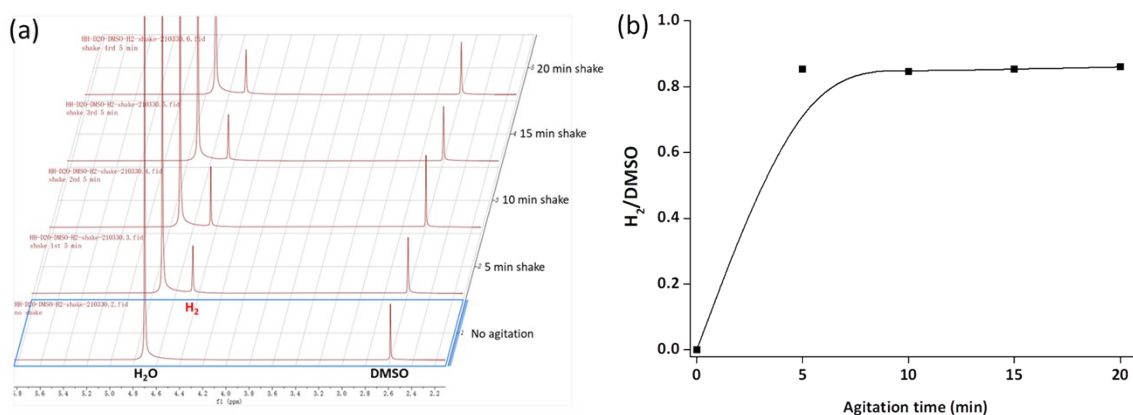


Fig S12. (a) NMR spectra of dissolved H_2 in D_2O at $20^\circ C$ as a function of agitation time. (b) H_2 solubility at $20^\circ C$ as a function of agitation time.

After the NMR tube is filled with 5 bar H_2 , it was shaken under constant pressure to check the agitation effect. As shown in **Fig S12b**, the agitation plays a key role in the dissolution of H_2 in D_2O most probably due to the low cross section area to depth ratio of the NMR tube. The gas diffusion in solvent is greatly improved by vigorous shaking (up-side down). In each measurement below, 20 min stirring is used to eliminate the influence of diffusion.

N₂ promoting effect at 20 °C

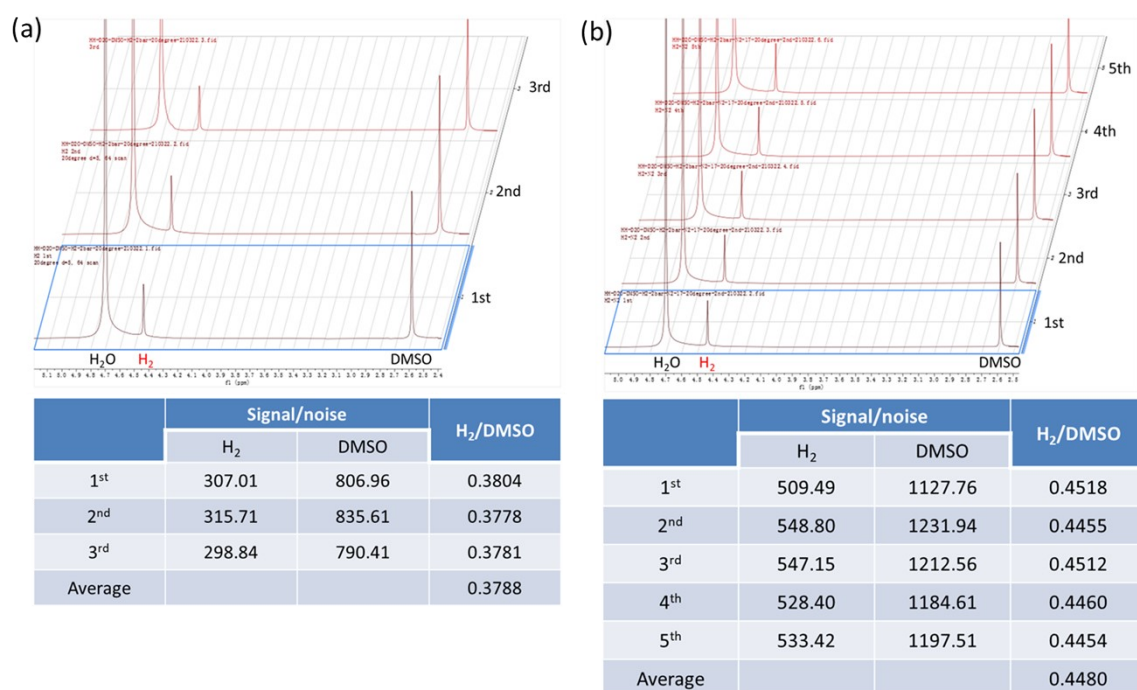
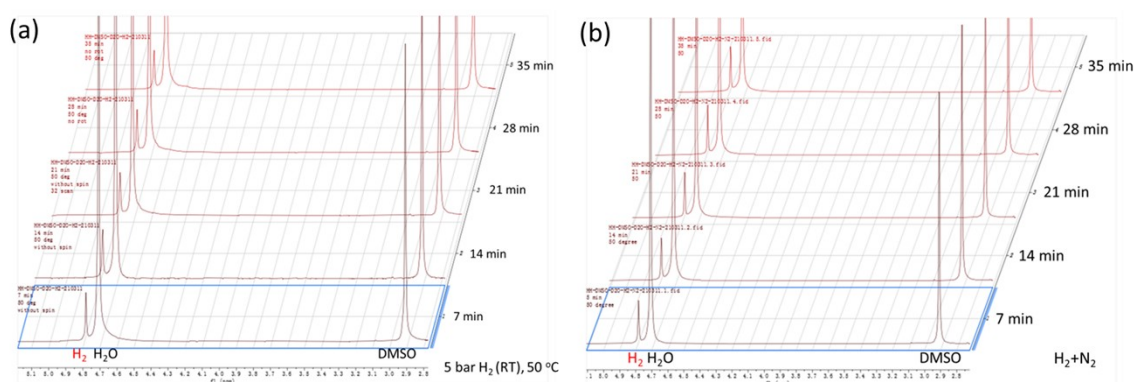


Fig S13. (a) H₂ solubility in D₂O under 2.02 bar H₂ in the absence of N₂. (b) H₂ solubility in D₂O under 2.18 bar H₂ in the presence of 17.11 bar N₂.

To compare H₂ only with H₂+N₂, the solvent remained unchanged in order to keep constant the DMSO concentration. The measurements were repeated for 3 or 5 times to reduce the error of the solubility measurements. The promoting effect of N₂ is determined to be 9.6% after the normalization with the H₂ pressure.

N₂ promoting effect at 50 °C



	Time(min)	7	14	21	28	35	Average	Rel. Ratio
H ₂ /DMSO	H ₂	0.1631	0.1617	0.1612	0.1598	0.1611	0.1614	100%
	H ₂ +N ₂	0.1756	0.1703	0.1664	0.1673	0.1692	0.1698	105.2%

Fig S14. (a) H₂ solubility in D₂O under 5.13 bar H₂ in the absence of N₂ recorded as a function of time. (b) H₂ solubility in D₂O under 5.13 bar H₂ in the presence of 10.19 bar N₂ recorded as a function of time. Scan number=32.

Both measurements are recorded at an interval of 7 min. It can be seen that the kinetic effect on H₂ dissolution under such conditions is not obvious. After the measurement with H₂, N₂ was directly introduced into the tube without removing H₂, and the tube was shaken for 20 min. The promoting effect of N₂ was determined to be 5.2 %.

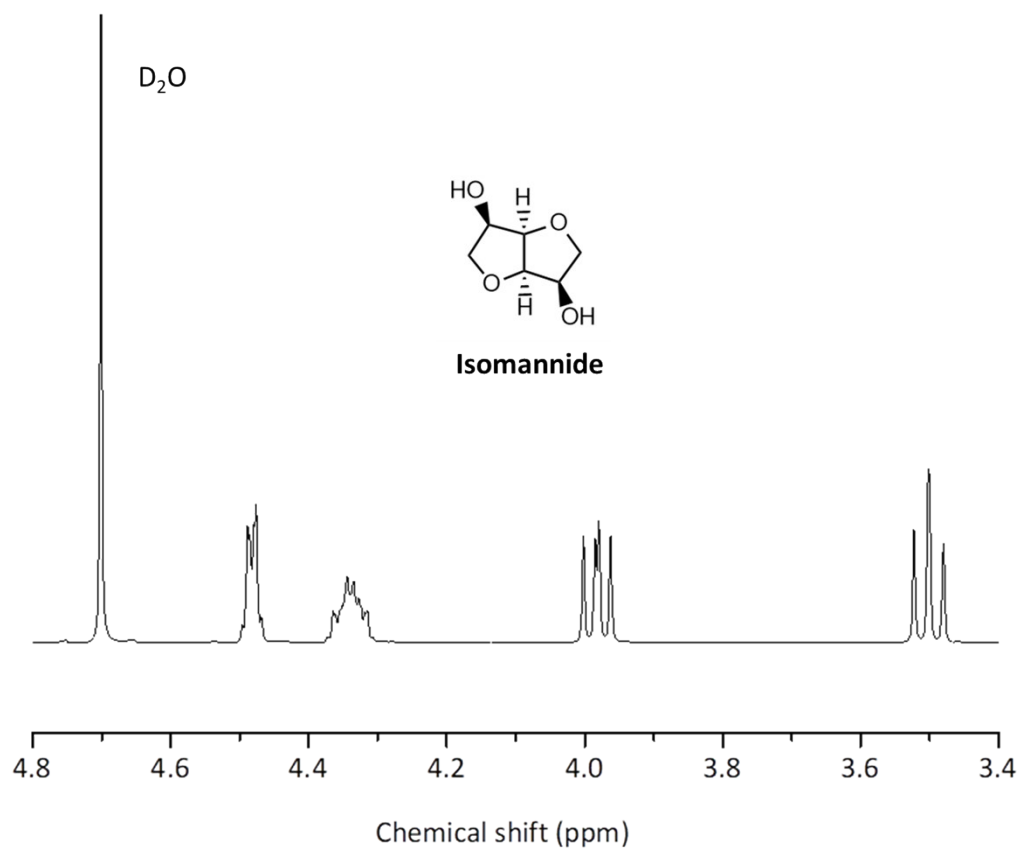


Fig S15. $^1\text{H-NMR}$ spectrum of isomannide in D_2O .

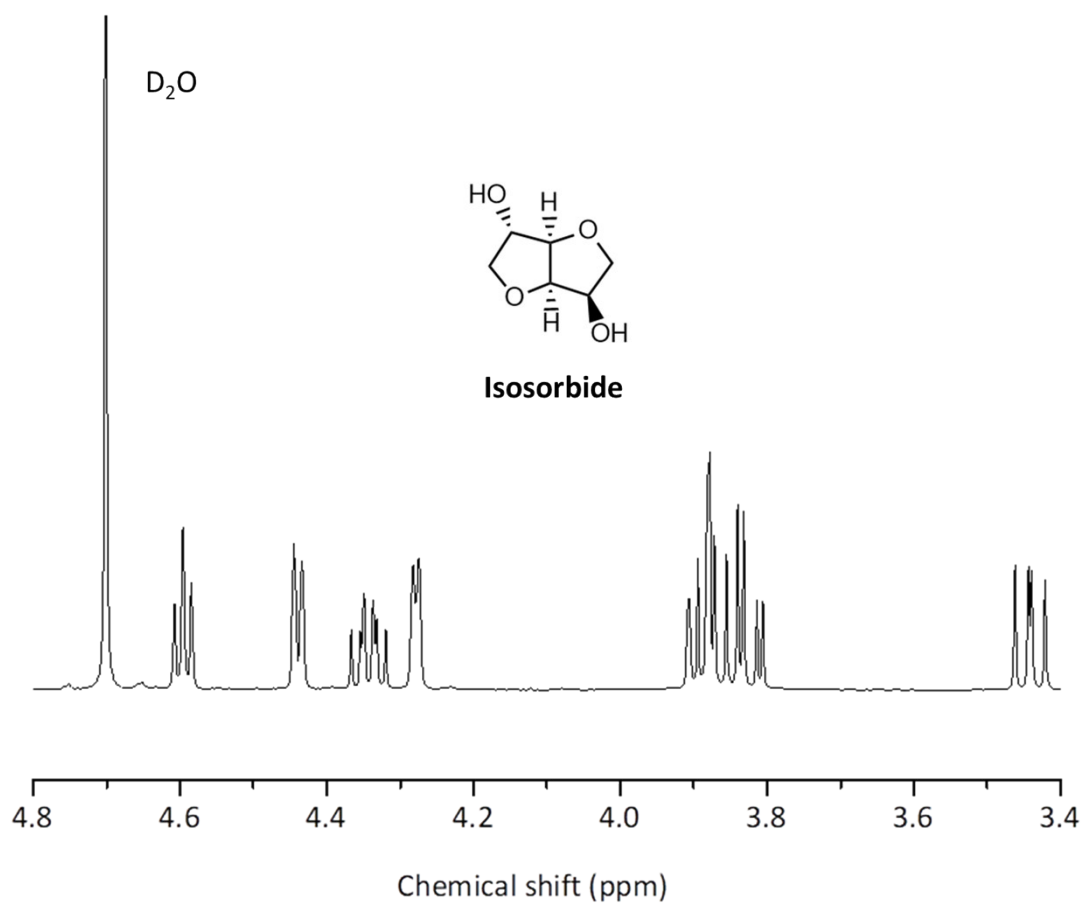


Fig S16. $^1\text{H-NMR}$ spectrum of isosorbide in D_2O .

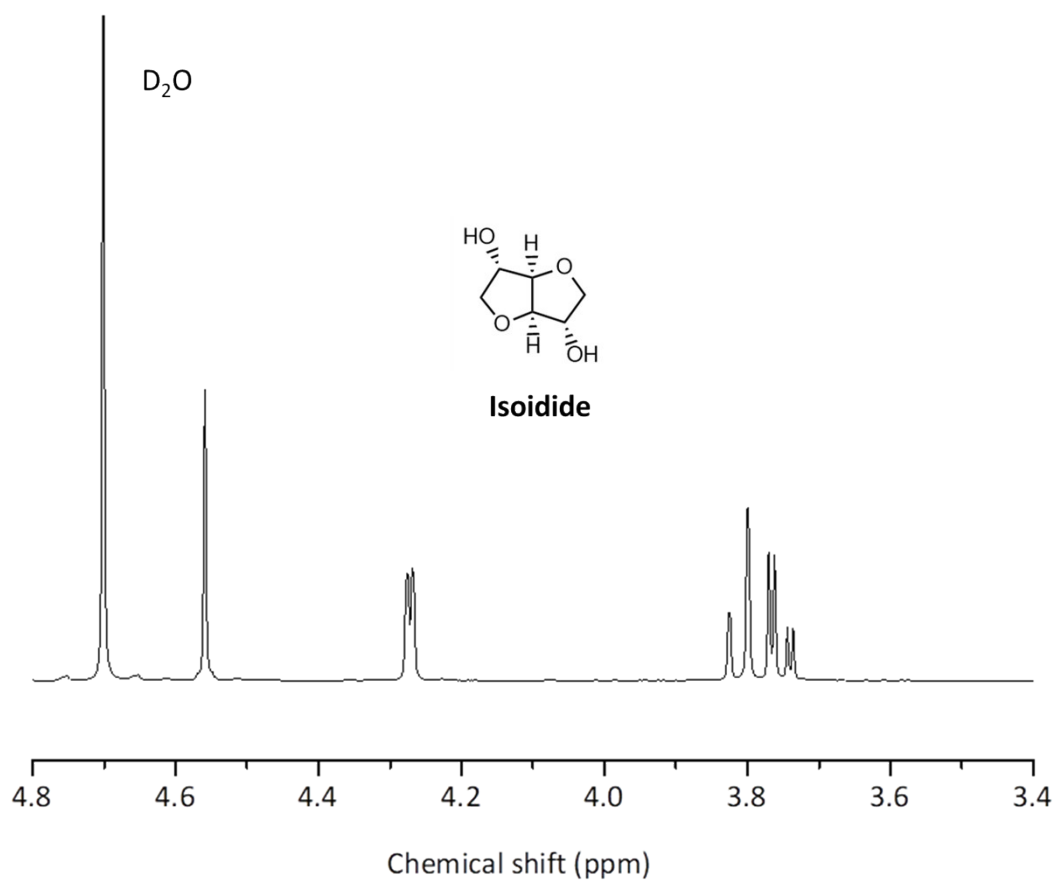


Fig S17. $^1\text{H-NMR}$ spectrum of isoidide in D_2O .

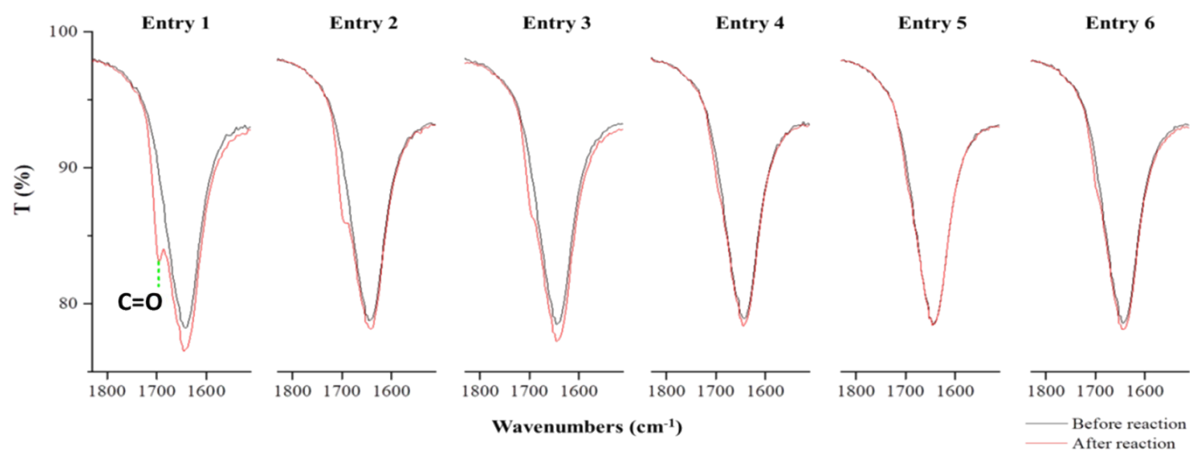
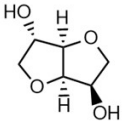
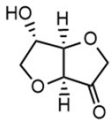
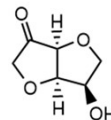
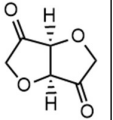
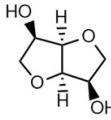
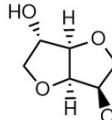
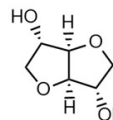
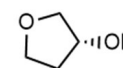
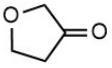
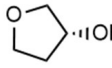
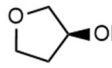


Fig S18. IR spectra of reaction mixtures after isomerisation in H₂O/IPA. Reaction conditions are in agreement with those in **Table S1**.

The band around 1698 cm⁻¹ is attributed to the C=O double bond of acetone.

Table S1. Isomerisation of isohexides and 3-OH-THF under H₂

Sub	γ (ketone)			γ (isomers)			CB (%)
	 trace	 0.0 %	 0.0 %	 3 %	 25 %	 38 %	66
	 trace			 52 %		 46 %	98

Reaction conditions: 1 g substrate, 15 mL H₂O, 0.05 g Ru/C, 30 bar H₂, 200 °C, 2h.

The ratio between endo/exo-OH-THF was determined by polarimeter.

Table S2. Isomerization of isohexides and 3-OH-THF under N₂

Sub	y(ketone)			y(isomers)			CB (%)
	trace	0.0 %	0.0 %	0.0 %	99.9 %	0.4 %	100.3
		2.3 %		89.5 %		0.0 %	91.8

Reaction conditions: 1 g substrate, 15 mL H₂O, 0.05 g Ru/C, 1 bar N₂, 200 °C, 2h.

The ratio between *endo/exo*-OH-THF was determined by polarimeter.

Table S3. Isomerisation in water/IPA mixture

Entry	Sub	Solvent (vol%)		T (°C)	t (h)	Pressure (bar)			IPA loss (%)	Ratio IS:II:IM	CB (%)
		H ₂ O	IPA			Start (N ₂)	at target T	After reaction			
1	IS	60%	40%	200	2	2	32	10	13	73 : 22 : 5	109
2	IS	60%	40%	160	2	2	14	5.3	5	97 : 3 : 0	98
3	IS	60%	40%	160	12	2	14	4.7	15	83 : 14 : 4	114
4	IS	60%	40%	120	2	2	6	3.1	1	98 : 2 : 0	104
5	IS	60%	40%	120	12	2	6	2.9	4	90 : 8 : 2	107
6	-	60%	40%	120	2	2	6	3.1	5	-	-

Reaction conditions: 1 g IS, 15 mL solvent, 0.05 g Ru/C

As shown in **Table S3**, several temperatures (200, 160, 120 °C) and reaction times (2 or 12 h) were applied to check if the dehydrogenation could be avoided in the isomerisation reaction. However, the pressure increase and the generated acetone are always observed and isomerisation kinetics is greatly slowed down due to the low temperature. By extending the reaction from 2 h to 12 h at 160 °C (Entries 2&3), the pressure increase (H₂) stayed unchanged while more IPA loss is observed, which indicates there might be a direct hydrogen transfer from IPA to isohexides.

Modelling time-evolution of H₂ concentration: effect of N₂ concentration

Multicomponent diffusion within a stagnant layer

Diffusion in multicomponent systems of n species may be described by the Maxwell-Stefan (MS) equations^{9,10}

$$d_i = \sum_{j=1}^n \frac{(x_i J_j - x_j J_i)}{c_t \mathfrak{D}_{ij}} \quad i=1, \dots, n \quad (S2)$$

where \mathfrak{D}_{ij} is the Maxwell-Stefan diffusivity between species i and j and has the physical significance of an inverse drag coefficient, c_t is the total concentration, and J_i and x_i refer to the molecular flux and molar fraction of species i , respectively. In eq S2, d_i , which can be considered as the driving force, can be expressed as follows

$$d_i \equiv \frac{x_i}{RT} \nabla_{T,P} \mu_i = \frac{x_i}{RT} \nabla \mu_i \quad (S3)$$

The subscripts T,P are used to emphasize that the gradient in eq S3, $\nabla = (\partial/\partial x, \partial/\partial y, \partial/\partial z)$, is to be calculated under constant temperature and pressure conditions.

The driving force, d_i , reduces to ∇x_i for ideal systems. Also, the sum of the n driving forces vanishes according to the Gibbs-Duhem relationship. The mathematical proofs are provided below

$$d_i \equiv \frac{x_i}{RT} \nabla \mu_i = \frac{x_i}{RT} \nabla [\mu_{i,0} + RT \ln(x_i)] = x_i \nabla [\ln(x_i)] = x_i \frac{\nabla x_i}{x_i} = \nabla x_i \quad (S4)$$

$$\sum_{i=1}^n d_i = \sum_{i=1}^n \frac{x_i}{RT} \nabla \mu_i = \sum_{i=1}^n \nabla x_i = 0 \quad (S5)$$

The driving force can be related to the composition of the different species as follows¹¹

$$d_i = \sum_{j=1}^{n-1} \Gamma_{ij} \nabla x_j \quad (S6)$$

where the thermodynamic factors, Γ_{ij} , are defined by

$$\Gamma_{ij} = \delta_{ij} + x_i \left. \frac{\partial \ln \gamma_i}{\partial x_j} \right|_{T,P} \quad (S7)$$

where γ_i is the activity coefficient of species i in the mixture, and δ_{ij} is the delta Dirac function.

Introducing eq S6 into eq S2, the MS equations take the form

$$\sum_{j=1}^{n-1} \Gamma_{ij} \nabla x_j = \sum_{j=1}^n \frac{(x_i J_j - x_j J_i)}{c_t \mathfrak{D}_{ij}} \quad i,j=1, \dots, n \quad (S8)$$

Assuming that $\Gamma_{ii} \rightarrow 1$ and $\Gamma_{ij} \rightarrow 0$, eq S8 transforms then into eq S9

$$\nabla x_i = \sum_{j=1}^n \frac{(x_i J_j - x_j J_i)}{c_t \mathfrak{D}_{ij}} \quad i,j=1, \dots, n \quad (S9)$$

From eq S9, the Fick diffusivities can be estimated from the MS diffusivities using the following expression

$$D_{ij} = \mathfrak{D}_{ij} \Gamma_{ii} \approx \mathfrak{D}_{ij} \quad i,j=1,\dots,n \quad (S10)$$

Application of Maxwell-Stefan equations to a stagnant layer for a ternary system (H₂, N₂, water)

The MS equations can be used to model the gas diffusion of two gases (*e.g.*, H₂ and N₂) within a stagnant layer of solvent (*e.g.*, water). The ternary system H₂ (1) - N₂ (2) - water (3) can be modelled as follows:

$$\nabla x_1 = \frac{(x_1 J_2 - x_2 J_1)}{c_t \mathfrak{D}_{12}} + \frac{(x_1 J_3 - x_3 J_1)}{c_t \mathfrak{D}_{13}} \quad (S11)$$

$$\nabla x_2 = \frac{(x_2 J_1 - x_1 J_2)}{c_t \mathfrak{D}_{12}} + \frac{(x_2 J_3 - x_3 J_2)}{c_t \mathfrak{D}_{23}} \quad (S12)$$

$$\nabla x_3 = -\nabla x_1 - \nabla x_2 \quad (\text{according to eq S5}) \quad (S13)$$

Taking into account the following equalities

$$x_1 + x_2 + x_3 = 1 \quad (S14)$$

$$J_1 + J_2 + J_3 = 0 \quad (\text{absence of convection}) \quad (S15)$$

Eqs S11 and S12 transform into the following expressions:

$$-\nabla x_1 = \frac{(x_2 J_1 - x_1 J_2)}{c_t \mathfrak{D}_{12}} + \frac{[x_1 J_2 + (1-x_2)J_1]}{c_t \mathfrak{D}_{13}} \quad (S16)$$

$$-\nabla x_2 = \frac{(x_1 J_2 - x_2 J_1)}{c_t \mathfrak{D}_{12}} + \frac{[x_2 J_1 + (1-x_1)J_2]}{c_t \mathfrak{D}_{23}} \quad (S17)$$

Since we expect to work at much higher concentration of the inert gas, $x_2 \gg x_1$, we can reasonably assume that $x_2 J_1 \gg x_1 J_2$. Eqs S16 and S17 can be then simplified as follows:

$$-c_t \nabla x_1 \approx \left[\frac{x_2}{\mathfrak{D}_{12}} + \frac{(1-x_2)}{\mathfrak{D}_{13}} \right] J_1 \quad (S18)$$

$$-c_t \nabla x_2 \approx -x_2 \left[\frac{1}{\mathfrak{D}_{12}} - \frac{1}{\mathfrak{D}_{23}} \right] J_1 \rightarrow -c_t \nabla \ln x_2 = \left[\frac{1}{\mathfrak{D}_{12}} - \frac{1}{\mathfrak{D}_{23}} \right] J_1 \quad (S19)$$

Eq S18 shows that the gradient of H₂ (1) can be expressed as a function of the molar fraction of N₂ (2). If the molar fraction of N₂ increases, then the gradient of H₂ is expected to decrease, meaning that the H₂ concentration approaches that of the bulk solution. Note that, for isosorbide isomerisation, J_1 should not equal the reaction rate, since H₂ is not a reactant.

Besides, the MS diffusivity, \mathfrak{D}_{13} , is expected to be a function of the composition of the system. A Vignes-type relation can be proposed for multicomponent systems using MS diffusivities at infinite dilution^{12,13}

$$\mathfrak{D}_{13} = \prod_{k=1}^3 (\mathfrak{D}_{13, x_k \rightarrow 1})^{x_k} \quad k = 1 \dots 3 \quad (S20)$$

$$\mathfrak{D}_{12} = \prod_{k=1}^3 (\mathfrak{D}_{13, x_1 \rightarrow 1} \mathfrak{D}_{13, x_2 \rightarrow 1})^{1/2} \quad (S21)$$

Reactor modelling

Using the analysis above, we provide below a modelling of the reactor used in this study (Taiatsu), which was used in the isosorbide isomerisation tests. A scheme of the reactor is provided in **Fig S19**. The reaction was conducted in water (15 mL) using 1 g of IS, 100 mg of catalyst (5%Ru/C) and 0.1 mol NaOH at 200 °C. The reaction was conducted in the presence of 20 bar H₂ either including N₂ (30 bar) or not. Our purpose is to model the mass transfer of H₂ in the reactor and predict the effect of N₂ on the H₂ concentration.

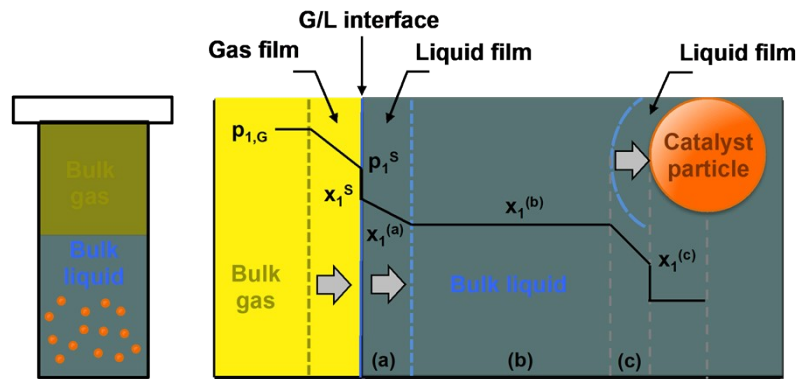


Fig S19. Left, scheme of the reactor used in this study; right, stagnant layer in the reactor, defining zones (a), (b) and (c).

In the analysis below, the reactor has been divided in three zones: (a) G-L contact, (b) bulk reactor, and (c) catalyst surface. We assume that the physical processes in zones (a) and (c) proceed by pure diffusion, whereas the reactor in zone (b) is perfectly stirred (i.e. the concentration is equal in all the points).

Modelling H₂ diffusion within the stagnant layer at the G-L interface [zone (a)]

Mass transfer of H₂ within zone (a) can be described using eq S18

$$-c_t D_{13} \nabla x_1^{(a)} = [1 - x_2^{(a)}] J_1^{(a)} \quad (S22)$$

with $z = 0 \rightarrow x_1^{(a)} = x_1^0$ (saturation at T= 200 °C, $p_{H_2} = 20$ bar)

Assuming that Γ_{11} is independent of $x_1^{(a)}$ and that $x_2^{(a)}$ (N₂) is almost constant and approaching the saturation value (x_2^s), eq S22 can be integrated as follows (steady-state regime)

$$J_1^{(a)} = c_t \frac{D_{13}}{(1 - x_2^s) l_a} [x_1^s - x_1^{(a)}] \quad (S23)$$

Modelling H₂ diffusion within the stagnant layer on the catalyst surface [zone (c)]

Mass transfer of H₂ within zone (c) can also be described using eq S19

$$-c_t D_{13} \nabla x_1^{(c)} = (1 - x_2^s) J_1^{(c)} \quad (S24)$$

with $z = 0 \rightarrow x_1^{(c)} = x_1^{(b)}$ (saturation at T= 200 °C, $p_{H_2} = 20$ bar)

A non-steady state mass balance can be established with the catalyst surface accounting for H₂ adsorption (linear regime)

$$J_1^{(c)} S_{\text{BET}} = KW \frac{dx_1^{(c)}}{dt} \quad (\text{S25})$$

with $t = 0 \rightarrow x_1^{(c)} = 0$ (degassed catalyst).

In eq S25, S_{BET} is the specific surface area of the catalyst (10 m²/g) and W is the saturation loading of H₂ (0.5 mmol/g according to the Ru loading on the catalyst and assuming 50% metal dispersion).

By combining eq S24 and eq S25, the following expression can be established

$$\frac{\mathcal{D}_{13}}{(1-x_2^s)\ell_c} [x_1^{(b)} - x_1^{(c)}] S_{\text{BET}} = KW \frac{dx_1^{(c)}}{dt} \quad (\text{S26})$$

Assuming that $x_2^{(a)}$ (N₂) is almost constant and approaching the saturation value (x_2^s), eq S26 can be integrated as follows

$$\frac{\mathcal{D}_{13} S_{\text{BET}}}{(1-x_2^s)KW\ell_c} t = \Phi t = -\ln \left[\frac{x_1^{(b)} - x_1^{(c)}}{x_1^{(b)}} \right] \text{ or } [x_1^{(b)} - x_1^{(c)}] = x_1^{(b)} \exp(-\Phi t) \quad (\text{S27})$$

with $\Phi = \frac{\mathcal{D}_{13} S_{\text{BET}}}{(1-x_2^s)KW\ell_c}$ (S28)

Time-evolution of the H₂ concentration in the reactor

The H₂ concentration in the reactor can be modelled using a macroscopic mass balance

$$J_1^{(a)} S_{\text{G-L}} - J_1^{(c)} S_{\text{BET}} m_{\text{cat}} = \frac{dn_1^{(b)}}{dt} \quad (\text{S29})$$

with $t = 0 \rightarrow x_1^{(b)} = 0$ (degassed catalyst).

In eq S29, $G_{\text{G-L}}$ accounts for the gas-liquid interfacial area and m_{cat} is the amount of catalyst in the reactor. Introducing eq S23 and eq S27 into eq S29, the following expression can be obtained considering that $x_1^{(a)} = x_1^{(b)}$ (perfect mixing)

$$\frac{\mathcal{D}_{13}}{(1-x_2^s)\ell_a} [x_1^s - x_1^{(b)}] a_{\text{G-L}} V - \frac{\mathcal{D}_{13}}{(1-x_2^s)\ell_c} x_1^{(b)} \exp(-\Phi t) S_{\text{BET}} m_{\text{cat}} = V \frac{dx_1^{(b)}}{dt} \quad (\text{S30})$$

where $a_{\text{G-L}}$ is the specific surface area [m².m⁻³], which dependent on the reactor hydrodynamics (i.e. mixing level).

Eq S30 can be simplified as follows

$$\frac{\mathcal{D}_{13}}{(1-x_2^s)\ell_a} \left[[x_1^s - x_1^{(b)}] \frac{a_{\text{G-L}}}{\ell_a} - x_1^{(b)} \exp(-\Phi t) \frac{S_{\text{BET}} m_{\text{cat}}}{V \ell_c} \right] = \frac{dx_1^{(b)}}{dt} \quad (\text{S31})$$

Eq S31 was solved numerically using finite differences. **Fig S19** plots the time-evolution of the H₂ concentration in the reactor at 20 bar H₂ as a function of the H₂ MS diffusivity estimated using eq S22 both in the absence and presence of 30 bar N₂, and the value of the specific surface area. The $\mathcal{D}_{ij,xk \rightarrow 1}$

diffusivities at infinite dilution were approached to Fick diffusivities and obtained from the literature.^{14,15} The calculations are provided below:

$$\begin{aligned} \text{Absence of } N_2: \mathfrak{D}_{13} &= (\mathfrak{D}_{13,x_1 \rightarrow 1})^{x_1} (\mathfrak{D}_{13,x_3 \rightarrow 1})^{x_3} \approx (\mathfrak{D}_{13,x_1 \rightarrow 1})^{x_1} (\mathfrak{D}_{13,x_3 \rightarrow 1})^{x_3} = \\ &= (4.0 \times 10^{-5})^{0.0005} (2.17 \times 10^{-9})^{0.9995} = 2.18 \times 10^{-9} \text{ m}^2 / \text{s} \end{aligned}$$

$$\begin{aligned} \text{Presence of } N_2: \mathfrak{D}_{13} &\approx (\mathfrak{D}_{13,x_1 \rightarrow 1})^{x_1} (\mathfrak{D}_{13,x_2 \rightarrow 1})^{x_2} (\mathfrak{D}_{13,x_3 \rightarrow 1})^{x_3} = (\mathfrak{D}_{13,x_1 \rightarrow 1})^{x_1} (\mathfrak{D}_{13,x_2 \rightarrow 1})^{x_2} (\mathfrak{D}_{13,x_3 \rightarrow 1})^{x_3} = \\ &= (4.0 \times 10^{-5})^{0.0005} (2.17 \times 10^{-9})^{0.9935} (2.5 \times 10^{-5})^{0.006} = 2.31 \times 10^{-9} \text{ m}^2 / \text{s} \end{aligned}$$

$$\mathfrak{D}_{12} = [(\mathfrak{D}_{13,x_3 \rightarrow 1})(\mathfrak{D}_{23,x_3 \rightarrow 1})]^{1/2} = [(2.17 \times 10^{-9})(1.5 \times 10^{-9})]^{1/2} = 1.80 \times 10^{-9} \text{ m}^2 / \text{s}$$

The trends plotted in **Fig S19** suggest that G-L mass transfer condition the H_2 solubility, especially for bad contactors (i.e. $l_a > 2.5$ mm). The introduction of N_2 is expected to enhance the H_2 solubility by a factor up to 10% by increasing the H_2 diffusivity. If the H_2 adsorption on the catalyst surface is very sensitive to the H_2 concentration, then this change, even if small, could condition the H_2 coverage on Ru. Besides, these calculations point out that, during the reaction time for isosorbide isomerisation (about 1 h), the H_2 concentration in the reactor can be about 10% the saturation value.

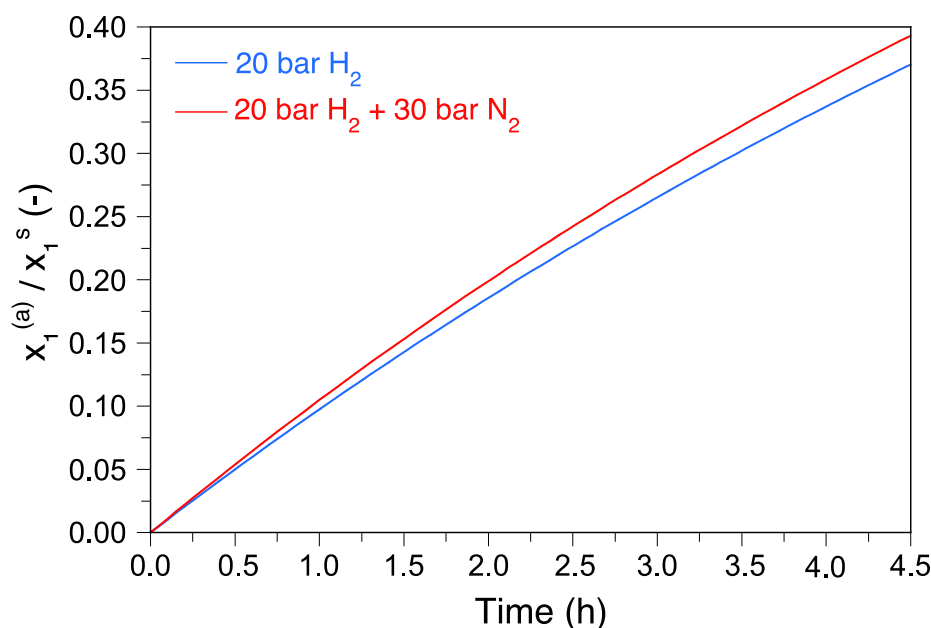


Fig S20. Time-evolution of the H_2 concentration in the reactor expressed as ratio between the molar fraction and saturation molar fraction of H_2 , computed both in the absence (blue curve) and presence of N_2 (red curve) by including the effect of N_2 on the H_2 MS diffusivity. Data for calculations: $V = 15$ mL, $a_{G-L} = 33 \text{ m}^2 \cdot \text{m}^{-3}$, $l_a = 100 \text{ } \mu\text{m}$, $K = 10^{-2} \text{ m}^3 / \text{mol}$, $W = 5 \times 10^{-4} \text{ mol Ru} / \text{g}_{\text{cat}}$, $m_{\text{cat}} = 100 \text{ mg}$, $S_{\text{BET}} = 10 \text{ m}^2 / \text{g}$, $l_c = 1 \text{ } \mu\text{m}$, $x_2^s = 6 \times 10^{-3}$.

In a second set of calculations, we considered that, in addition of the H_2 MS diffusivity, the specific surface area can be increased in the presence of N_2 . Indeed, the presence of a second gas at high

pressure can decrease the gas-liquid interfacial tension, generating bubbles of smaller size.^{16,17} In this view, if we consider that the specific surface area of our reactor increases by a factor of 2, then the H₂ solubility could be remarkably increased as depicted in Fig S20. Overall, we conclude that a second gas at high pressure can promote the H₂ solubility by increasing the H₂ diffusivity and the G-L surface area.

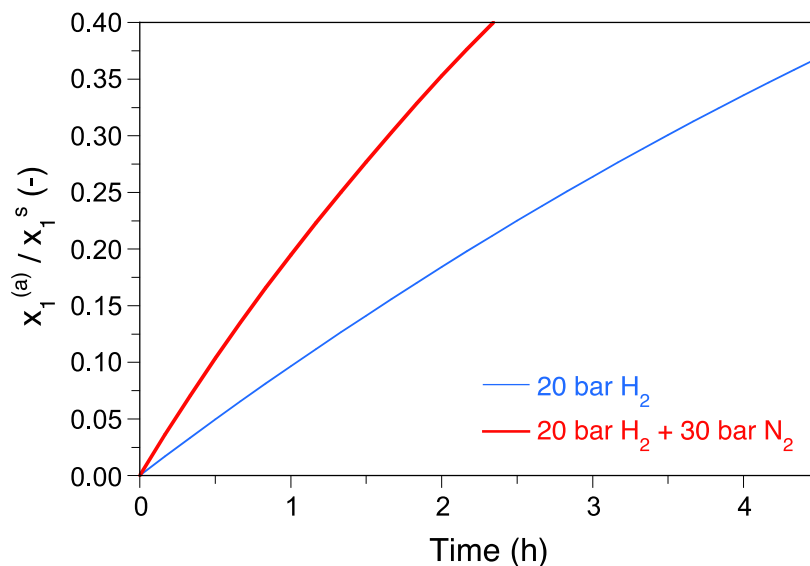


Fig S21. Time-evolution of the H₂ concentration in the reactor expressed as ratio between the molar fraction and saturation molar fraction of H₂, computed both in the absence (blue curve) and presence of N₂ (red curve) by including the effect of N₂ on the H₂ MS diffusivity and on the specific surface area due to the formation of bubbles. Data for calculations: V = 15 mL, a_{G-L} = 66 m².m⁻³, l_a = 100 μm, K = 10⁻² m³/mol, W = 5x10⁻⁴ mol Ru /g_{catr}, m_{cat} = 100 mg, S_{BET} = 10 m²/g, l_c = 1 μm, x₂^s = 6x10⁻³.

References

1. G. Kresse and J. Furthmüller, *J. Phys. Rev. B*, 1996, **54**, 11169.
2. J. P. Perdew, K. Burke and M. Ernzerhof, *Phys. Rev. Lett.*, 1996, **77**, 3865.
3. S. Steinmann and C. A. Corminboeuf, *J. Chem. Phys.*, 2011, **134**, 044117.
4. P. E. Blöchl, *Phys. Rev. B*, 1994, **50**, 17953.
5. G. Kresse and D. Joubert, *Phys. Rev. B*, 1999, **59**, 1758.
6. J. W. Arblaster, *Platinum Metals Rev.*, 2013, **57**, 127.
7. P. J. Feibelman, *Science*, 2002, **295**, 99.
8. H. Gilboa, B. Chapman and P. Kuchel, *J. Magn. Res., Series A*, 1996, **119**, 1.
9. R. Krishna and J. A. Wesselingh, *Chem. Eng. Sci.*, 1997, **52**, 861.
10. R. Taylor and R. Krishna, *Multicomponent Mass Transfer*, Wiley, New York, 1993.
11. H. A. Kooijman, R. Taylor, *Ind. Eng. Chem. Res.*, 1991, **30**, 1217.
12. A. Vignes, *Ind. Eng. Chem. Res. Fundam.*, 1966, **5**, 189.
13. J. A. Wesselingh, R. Krishna, *Elements of Mass Transfer*, Ellis Horwood: Chichester, UK, 1990.
14. J. H. Hildebrand, R. H. Lamoreaux, *Proc. Nat. Acad. Sci. USA*, 1974, **71**, 3321.
15. A. Akgerman, J. L. Gainer, *Ind. Eng. Chem. Fundam.*, 1972, **11**, 373.
16. M-Y. Chang, J. G. Eiras, B. I. Morsi, *Chem. Eng. Process.*, 1991, **29**, 49.
17. M-Y. Chang, B. I. Morsi, *Chem. Eng. Sci.*, 1992, **47**, 1779.